Robust Ferromagnetism in Highly Strained $SrCoO_3$ Thin Films

Yujia Wang,[1,2] Qing He,[3,*] Wenmei Ming,[4] Mao-Hua Du,[4] Nianpeng Lu,[1,5] Clodomiro Cafolla,[3] Jun Fujioka,[6]
Qinghua Zhang,[5,7] Ding Zhang,[1,2] Shengchun Shen,[1,2] Yingjie Lyu,[1,2] Alpha T. N'Diaye,[8] Elke Arenholz,[8]
Lin Gu,[5] Cewen Nan,[7] Yoshinori Tokura,[9,10] Satoshi Okamoto,[4,†] and Pu Yu[1,2,9,‡]

[1] *State Key Laboratory of Low Dimensional Quantum Physics and Department of Physics,*
Tsinghua University, Beijing, 100084, China
[2] *Frontier Science Center for Quantum Information, Beijing, 100084, China*
[3] *Department of Physics, Durham University, Durham DH1 3LE, United Kingdom*
[4] *Materials Science and Technology Division, Oak Ridge National Laboratory,*
Oak Ridge, Tennessee 37831, USA
[5] *Beijing National Laboratory for Condensed Matter Physics, Institute of Physics,*
Chinese Academy of Science, Beijing 100190, China
[6] *Graduate School of Pure and Applied Science, University of Tsukuba, Tsukuba, Ibaraki, Japan*
[7] *State Key Laboratory of New Ceramics and Fine Processing, School of Materials Science*
and Engineering, Tsinghua University, Beijing 100084, China
[8] *Advanced Light Source, Lawrence Berkeley National Laboratory, Berkeley, California 94720, USA*
[9] *RIKEN Center for Emergent Matter Science (CEMS), Wako, Saitama 351-0198, Japan*
[10] *Tokyo College and Department of Applied Physics, University of Tokyo, Tokyo 113-8656, Japan*

(Received 24 September 2019; revised manuscript received 17 January 2020; accepted 27 February 2020; published 7 May 2020)

Epitaxial strain provides important pathways to control the magnetic and electronic states in transition-metal oxides. However, the large strain is usually accompanied by a strong reduction of the oxygen-vacancy formation energy, which hinders the direct manipulation of their intrinsic properties. Here, using a postdeposition ozone annealing method, we obtain a series of oxygen stoichiometric $SrCoO_3$ thin films with the tensile strain up to 3.0%. We observe a robust ferromagnetic ground state in all strained thin films, while interestingly the tensile strain triggers a distinct metal-to-insulator transition along with the increase of the tensile strain. The persistent ferromagnetic state across the electrical transition therefore suggests that the magnetic state is directly correlated with the localized electrons, rather than the itinerant ones, which then calls for further investigation of the intrinsic mechanism of this magnetic compound beyond the double-exchange mechanism.

DOI: 10.1103/PhysRevX.10.021030

Subject Areas: Condensed Matter Physics, Magnetism,
Materials Science

I. INTRODUCTION

In complex oxides, the epitaxial strain in thin film structures provides an essential control parameter to manipulate their corresponding electronic and magnetic ground states due to the interplay among lattice, charge, orbital, and spin degrees of freedom. A large group of transition-metal-oxide materials have demonstrated the emergence of novel properties through strain engineering, such as enhanced transition temperatures in ferroelectric [1], ferromagnetic (FM) [2], and superconducting [3] orders, as well as emergent exotic electronic states [4–6], as widely reported in high-quality epitaxially strained thin films.

Among such an oxide-materials family, particular attention has been payed to perovskite $SrCoO_3$ recently due to its intriguing FM metallic ground state [7,8] in the bulk compound attributed to the double-exchange mechanism proposed by Zener [9]. The density functional theory (DFT) calculations proposed that the Co d^6 ion antiferromagnetically couples with the ligand hole in the surrounding oxygen p states through the p-d hybridization to form the intermediate spin Co d^6L state [10,11]. More sophisticated treatment of the correlation effects, using the DFT + dynamical mean field theory (LDA + DMFT) [12], claimed that the local moment in $SrCoO_3$ results from the coherent superposition of different atomic states rather than the intermediate spin state [13]. Motivated by the

---

[*] qing.he@durham.ac.uk
[†] okapon@ornl.gov
[‡] yupu@mail.tsinghua.edu.cn

possible multiferroicity in strained transition-metal oxides [14], the magnetic ground state of strained $SrCoO_3$ was studied using the standard DFT. It was predicted that the ground state changes from a FM metallic state to an antiferromagnetic (AFM) metallic state, with a moderate tensile strain of 2.0% [15,16]. These theoretical predictions triggered a series of experimental studies to examine epitaxially strained $SrCoO_3$ thin films [17–20]. While most groups have obtained the FM metallic state in $SrCoO_3$ at low strain states, results on highly tensile-strained samples showed large diversity, which is likely due to the lack of good oxygen stoichiometry of the material resulting from the reduction of the oxygen-vacancy formation energy due to large tensile strains [17,18,21]. Thus, the intrinsic magnetic and electronic states as well as the underlying mechanism of highly strained $SrCoO_3$ still remain elusive.

In this paper, we report our magnetic study of highly strained $SrCoO_3$ thin films (up to tensile strain of ∼3.0%) with excellent oxygen stoichiometry, which is achieved by a new postdeposition ozone annealing process. To our surprise, the robust FM ground state is found in all tensile strained thin films, which is in stark contrast to previous theoretical predictions and experimental reports claiming a transition to the AFM state. Interestingly, we observe a metal-to-insulator transition along with the increase of the tensile strains. To gain insight into this observation, we carry out DFT + DMFT calculations and find that the orbital occupation changes more strongly with strain than what DFT predicts. Based on this, we propose a superexchange mechanism with alternating orbital ordering, which is consistent with the robust FM ground state with insulating transport.

II. RESULTS

A. Fabrication and characterization of highly strained $SrCoO_3$ thin films

In previous studies, the strained $SrCoO_3$ samples were typically achieved via *in situ* oxygen (or low-pressure ozone) annealing processes, in which the resulting samples usually possess pronounced oxygen-vacancy contents. In this study, a two-step method has been developed to achieve the desired high-quality epitaxial thin films with great oxygen stoichiometry. First, the brownmillerite $SrCoO_{2.5}$ thin films (∼30 nm) are grown using the pulsed laser deposition method, and then they are postannealed within ozone (see details in Sec. IV). The elevated annealing temperature (∼300 °C) and high ozone content (5 g/m^3 in 1 bar O_2) triggers effectively the phase transformation from brownmillerite to perovskite with excellent oxygen stoichiometry of $SrCoO_3$ [Fig. 1(a)].

To manipulate the epitaxial strain state, various substrates, (001)-oriented single crystal $La_{0.3}Sr_{0.7}Al_{0.65}Ta_{0.35}O_3$ (LSAT) ($a = 0.3868$ nm), $SrTiO_3$ (STO) ($a = 0.3905$ nm), and $(110)_o$-oriented $DyScO_3$ (DSO) ($a_{\mathrm{pseudocubic}} = 0.3944$ nm), are carefully selected, providing tensile strains of 1.0%, 2.0%, and 3.0% with respect to the lattice constant (0.3829 nm) of bulk $SrCoO_3$ [7]. As a consequence, the as-grown $SrCoO_{2.5}$ samples are epitaxially strained on all selected substrates and the crystalline orientations are perfectly correlated with that of the substrates underneath (see Supplemental Material Fig. S1 [22]). It is interesting to note that the oxygen-vacancy channels of brownmillerite align along the in-plane (out-of-plane) direction with compressive (tensile) strain states, as evidenced by the presence of the superlattice peaks in the x-ray diffraction (XRD) θ-2θ scans [starred peaks in Fig. 1(b)] only for the samples grown on LSAT and STO substrates with compressive strain.

Despite different oxygen-vacancy orientations, all samples can be nicely transformed into perovskite structure through postdeposition ozone annealing, where the CoO_4 tetrahedra are oxidized into the CoO_6 octahedra, reflecting in the XRD results as the complete absence of the superlattice peaks and the movement of the pseudocubic (001) and (002) diffraction peaks toward the higher angles. Furthermore, detailed x-ray reciprocal-space mappings (RSM) along the pseudocubic (103) direction [Fig. 1(c)] are carried out to investigate the epitaxial relationship between thin films and substrates, in which the identical horizontal $\boldsymbol{q}$ values between the films and substrates (marked with red-dashed lines) strongly suggest that the post-ozone-annealed $SrCoO_3$ thin films are coherently strained with substrates (see Supplemental Material Table S1 for lattice parameters [22]).

Conventionally, the tensile strain in fully strained samples would introduce a systematic lattice contraction along the film-normal direction. However, such a trend clearly breaks down for the film grown on DSO substrate, in which a clear lattice expansion is observed. We speculate that such a crystalline structure change might be related to the evolution of lattice symmetry with tensile strain. With STO and LSAT substrates, the samples would be strained into the tetragonal phase from its bulk cubic compound; while with DSO substrate, the lattice structure would be largely deformed into the orthorhombic phase with lower symmetry. It is interesting to note that a similar structural anomaly was also observed in the previous theoretical work [15], in which the lattice changes from a high symmetry $P4/mmm$ to a lower symmetry $Pmc2_1$ at ∼2% tensile strain. The high-quality epitaxial nature of $SrCoO_3$ thin films was further confirmed by the high-resolution transmission electron microscopy (HRTEM) study (see Supplemental Material Fig. S2 [22]), which ascertains that by this postdeposition ozone annealing method the $SrCoO_3$ thin films can be fully strained on the DSO substrates with as high as 3.0% strain without the formation of any detectable interfacial defects that would cause strain relaxation otherwise.

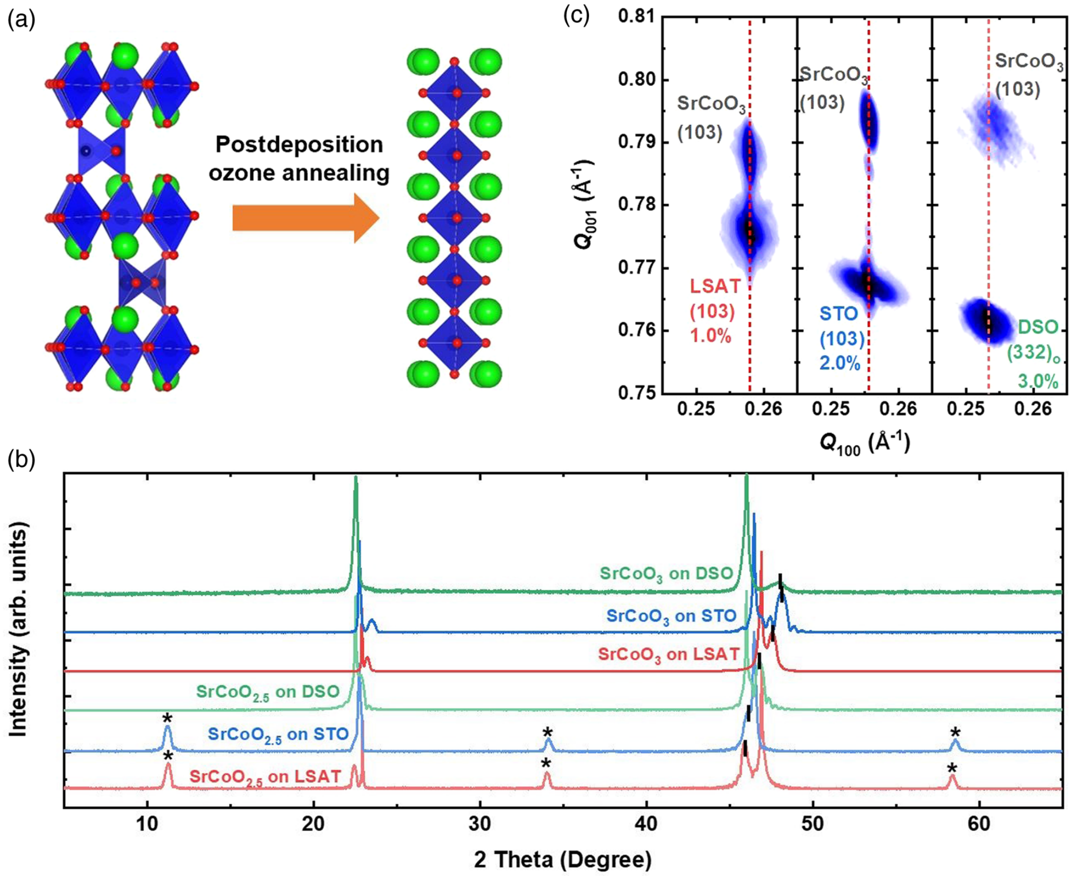

FIG. 1. Strain engineered $SrCoO_3$ thin films. (a) Schematic diagram of postdeposition ozone annealing induced phase transformation from $SrCoO_{2.5}$ to $SrCoO_3$. (b) X-ray diffraction θ-2θ scans of pristine $SrCoO_{2.5}$ and postdeposition ozone annealed $SrCoO_3$ thin films grown on LSAT (001), STO (001), and DSO $(110)_o$ substrates (with 1.0%, 2.0%, and 3.0% tensile strain, respectively). Superlattice peaks with star marks suggest that the oxygen-vacancy channel prefers in-plane orientation for the films grown on LSAT and STO substrates, while with postdeposition ozone annealing process the superlattice peaks are vanished for all films. (c) Reciprocal-space mapping along the pseudocubic (103) direction of $SrCoO_3$ thin films. The perfect alignment of the Q_{100} values between the thin films and the substrates is highlighted by the red-dashed lines, suggesting that the films are coherently strained by all the substrates.

As mentioned, the lack of stoichiometry of oxygen concentration in highly strained $SrCoO_3$ samples was a big challenge that researchers suffered in previous studies, where noticeable oxygen vacancies are always formed [18–20]. The presence of oxygen vacancies in thin films would strongly modify the corresponding valence states of Co ions as well as their hybridization with oxygen ions. Thus, in order to carefully evaluate the oxygen stoichiometry in our samples, we perform the valence-state-sensitive soft x-ray absorption spectroscopy (XAS) at both the Co L edges and oxygen K edge for all strained $SrCoO_3$ thin films. To avoid the influence of possible surface reduction, we employ a bulk sensitive fluorescence yield (FY) mode to collect the XAS signals. The XAS spectra at Co L edges [Fig. 2(a)] clearly reveal that all $SrCoO_3$ films show identical features with the characteristic Co^{4+} L_3 peak at ~780.8 eV. For reference, the L_3 peak of the pristine $SrCoO_{2.5}$ sample is found at ~780.3 eV with a very different line shape. This clear difference therefore suggests that the cobalt valance in all strained $SrCoO_3$ thin films is mostly 4+ and their oxygen stoichiometry difference is negligible. For comparison, previous studies reveal typically an energy shift of 0.3 eV, corresponding to the change of oxygen contents by ~0.15 per unit cell [18,20]. It is important to note that the surface-sensitive total electron yield (TEY) mode also provides consistent results (see Supplemental Material Fig. S3 [22]) as compared with the spectra taken with FY mode, indicating the homogeneity nature of the films along the growth direction. As the change of oxygen content can also modify the hybridization between O $2p$ and Co $3d$ orbitals, we further study the oxygen K-edge XAS spectra, in which identical hybridization features at ~527.6 eV (see Supplemental Material Fig. S4 [22]) further prove the excellent oxygen stoichiometry, since this hybridization peak in oxygen-deficient $SrCoO_{2.5}$ would be dramatically suppressed and shifted toward higher energy (~529.2 eV) [23,24]. With all of these careful analyses, we can confirm that the postdeposition ozone annealing method achieves coherently strained and stoichiometric $SrCoO_3$ thin films.

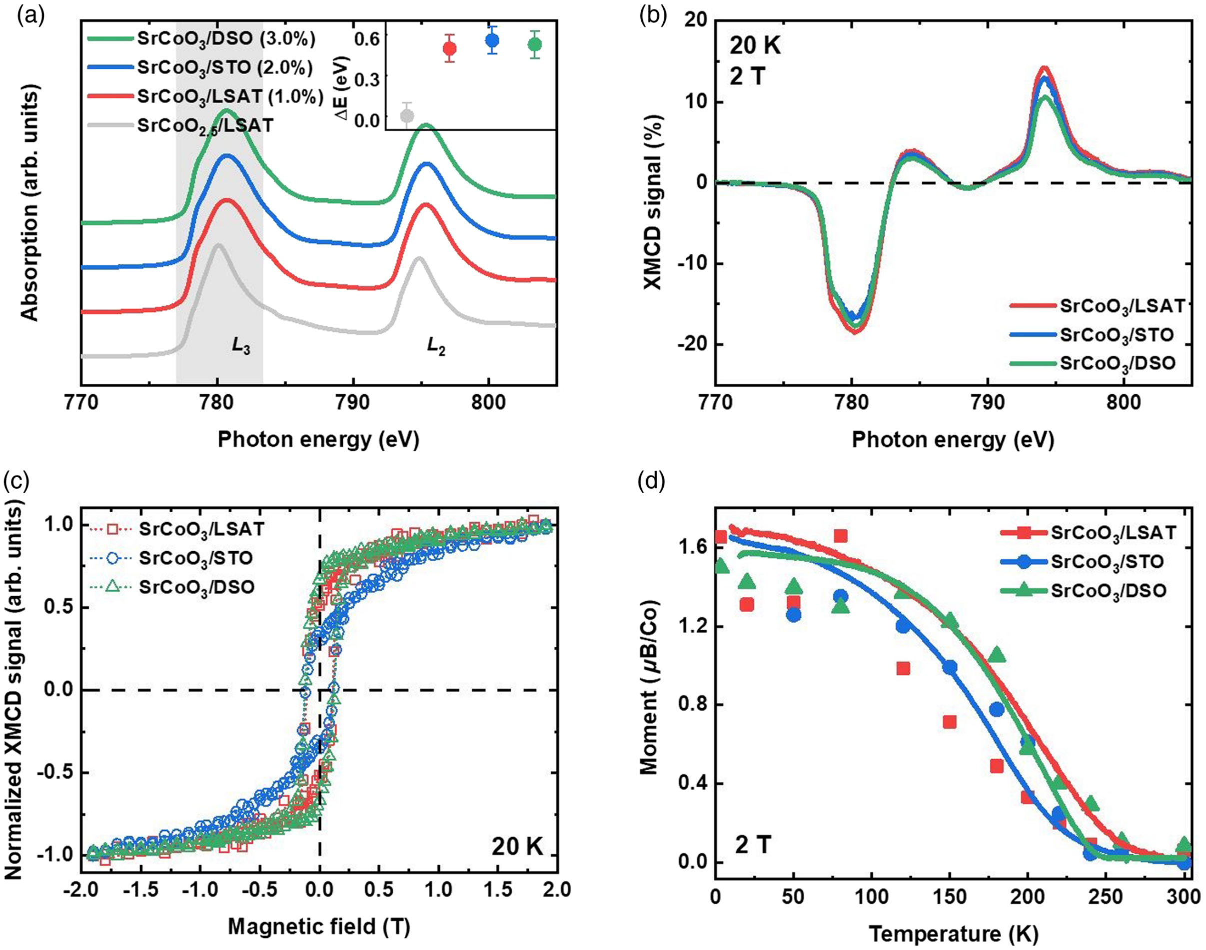

FIG. 2. Robust ferromagnetism in strained $SrCoO_3$ thin films. (a) Comparison of the Co L-edge x-ray absorption spectra taken using the fluorescence yield mode. The inset shows negligible peak shift (within the resolution of 0.1 eV) at the Co L_3 edge for all $SrCoO_3$ samples. (b) Co L-edge XMCD spectra taken from strain engineered $SrCoO_3$ thin films at 2 T and 20 K. (c) Magnetic-field-dependent XMCD signals for Co L_3 edge in strained $SrCoO_3$ thin films measured at 20 K. (d) Summary of the temperature-dependent magnetizations calculated by the XMCD sum rule (solid squares, circles, and triangles) and macroscopic magnetizations measured by SQUID (solid lines) (see Sec. IV) for $SrCoO_3$ thin films at various strain states.

B. Robust ferromagnetism in the highly strained samples

With these high-quality samples, we further investigate their intrinsic magnetic properties. Since the large paramagnetic background of DSO prohibits the direct magnetic measurement of the thin films grown on it, we carry out the element-specific and magnetic-resolved soft x-ray magnetic circular dichroism (XMCD) measurement [25]. Figure 2(b) shows the measured XMCD spectra of Co L edges at 20 K, in which the pronounced (~18% at L_3 edge) XMCD signals with similar characteristic peaks manifest that all strained $SrCoO_3$ thin films possess robust magnetizations. Figure 2(c) represents the magnetic-field-dependent XMCD for all three samples, which shows well-defined hysteresis loops, confirming the FM ground states. Using the XMCD sum rule (see Ref. [25] and Supplemental Material Fig. S5 [22]) we calculate the spin and orbital contributions for the total magnetization as being around $\sim 1.0\ \mu_B/\mathrm{Co}$ and $\sim 0.4\ \mu_B/\mathrm{Co}$, respectively. This result is consistent with the experimentally reported value for bulk $SrCoO_3$ [7] as well as slightly strained (1.0%) thin films [23,24], however, it is in disagreement with some previous theoretical calculations that predicted an AFM ground state for highly strained samples [15,16]. To further investigate the FM state, we carry out temperature-dependent XMCD measurement for all strained samples (see Supplemental Material Fig. S6 [22]) with the calculated total magnetizations summarized in Fig. 2(d), which are consistent with the macroscopically measured magnetizations. The magnetic transition temperatures are estimated to be ~250 K, which is consistent with the previously reported value in high-quality $SrCoO_3$ samples grown on LSAT [23,24,26].

C. Strain-induced metal-to-insulator transition

While showing similar and robust FM states, this series of strained $SrCoO_3$ samples exhibit very different electronic

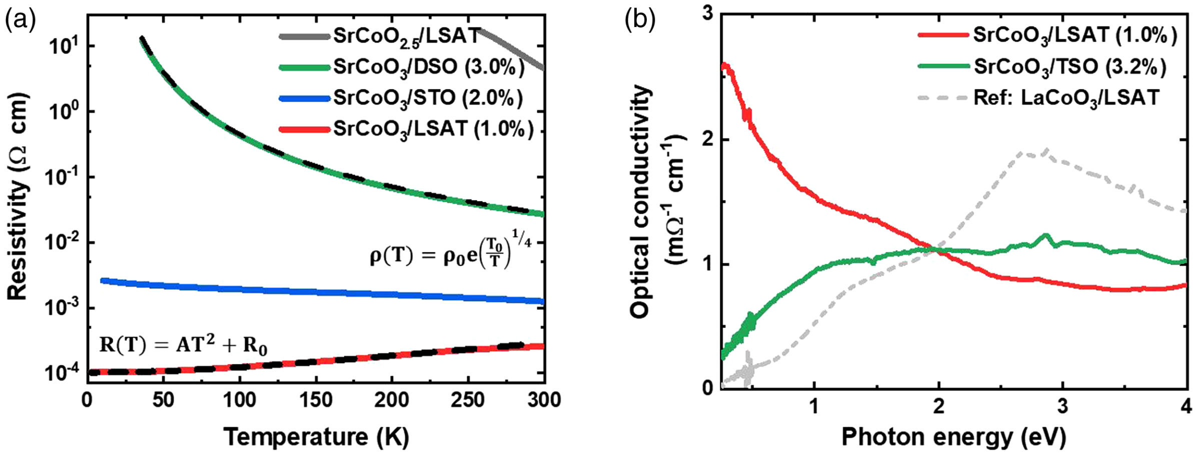

FIG. 3. Strain-induced metal-to-insulating transition in $\mathrm{SrCoO_3}$ thin films. (a) Temperature-dependent resistivity of strained $\mathrm{SrCoO_3}$ thin films grown on various substrates. The result of $\mathrm{SrCoO_{2.5}}$ grown on LSAT is shown in gray as reference. The fitting of the resistivity results are shown in dotted lines. (b) The room-temperature optical conductivity spectra from $\mathrm{SrCoO_3}$ thin films grown on LSAT (1.0%) and TSO (3.2%) substrates (we replaced the DSO substrate with TSO to avoid the absorption background from the DSO substrate.). The gray dotted line shows the result from a typically Mott insulator of $\mathrm{LaCoO_3}$ (grown on LSAT substrate) for comparison purpose.

properties, as revealed by the temperature-dependent electrical transport measurements shown in Fig. 3(a). The $\mathrm{SrCoO_3}$ sample grown on LSAT substrate shows a good metallic characteristic with residual resistivity of $\sim 10^{-4}\ \Omega\,\mathrm{cm}$ at ~15 K, which is much lower than previously reported values of single crystalline bulk [7] and thin films [24], however consistent with our recent studies of $\mathrm{SrCoO_3}$ thin films obtained with ionic liquid gating [26]. This fact again confirms that our ozone-annealed $\mathrm{SrCoO_3}$ samples are of high crystalline quality with minimal oxygen-vacancy concentration. This temperature-dependent curve follows nicely the T^2 relationship, in accordance with the Fermi liquid behavior of this metallic sample. Interestingly, with the increase of tensile stain, the conductivity is dramatically suppressed and a distinct insulating behavior is developed in the sample grown on DSO. Specifically, we have observed a more than 2 orders of magnitude enhancement of resistivity at room temperature between the LSAT and DSO samples. A careful analysis reveals that the temperature dependence of such a highly strained sample can be fitted with the three-dimensional Mott variable range hopping model [27,28] with $\rho(T) = \rho_0 e^{(T_0/T)^{1/4}}$. For $\mathrm{SrCoO_3}$ grown on STO with tensile strain at the intermediate state, the resistivity remains insensitive across a wide temperature range [blue line in Fig. 3(a)], indicating that the $\mathrm{SrCoO_3}$ film grown on STO is close to the phase boundary of metal insulator transition. For comparison, $\mathrm{SrCoO_{2.5}}$ thin film grown on the LSAT substrate shows a dramatically reduced room temperature conductivity as compared with all $\mathrm{SrCoO_3}$ thin films, and its exponential temperature dependence follows nicely the thermal activated semiconducting behavior.

To provide further insight into the strain-induced metal-to-insulator transition, we measure the optical conductivity spectra for selected $\mathrm{SrCoO_3}$ samples as shown in Fig. 3(b). A Drude-like feature is observed for the sample grown on the LSAT substrate, which is consistent with its metallic nature. To investigate the insulating state, we replace the DSO substrate with $\mathrm{TbScO_3}$ (TSO) ($a_{\mathrm{pseudocubic}} =$ 3.953 nm) with the strain of 3.2% to avoid the absorption background from the DSO substrate. With this sample, the Drude feature is significantly suppressed with a spectra weight transferred to higher photon energy, which clearly indicates an insulating state of the $\mathrm{SrCoO_3}$ with large strain. As a control experiment, reference spectra taken from a typical Mott insulator $\mathrm{LaCoO_3}$ (with $\mathrm{Co^{3+}}$), show a further shift of spectra weight toward higher photon energy with negligible spectra intensity at low energy. The notable spectral weight transfer over the large energy scale (~2 eV) between these samples at different strain states indicates that $\mathrm{SrCoO_3}$ is on the verge of the electron-correlation-induced metal-to-insulator transition or the Mott transition, critically driven by lattice strains [29].

With this evidence, we demonstrate experimentally a persistent FM state in highly strained $\mathrm{SrCoO_3}$ thin films with a metal-to-insulator transition occurring at a ~2.0% tensile strain state. In previous theoretical works, the FM state in $\mathrm{SrCoO_3}$ was usually attributed to the ferromagnetically coupled intermediate-spin Co $d^6\underline{L}$ through a Zener double-exchange mechanism [10,11], in which the FM ground state would be accompanied by a metallic electric state. This would lead to an immediate question regarding how the highly strained $\mathrm{SrCoO_3}$ thin films could maintain the FM ground state while undergoing a metal-to-insulator transition.

D. Electronic structure calculations

In order to understand the underlying mechanism, we performed DFT calculations as well as DFT + DMFT

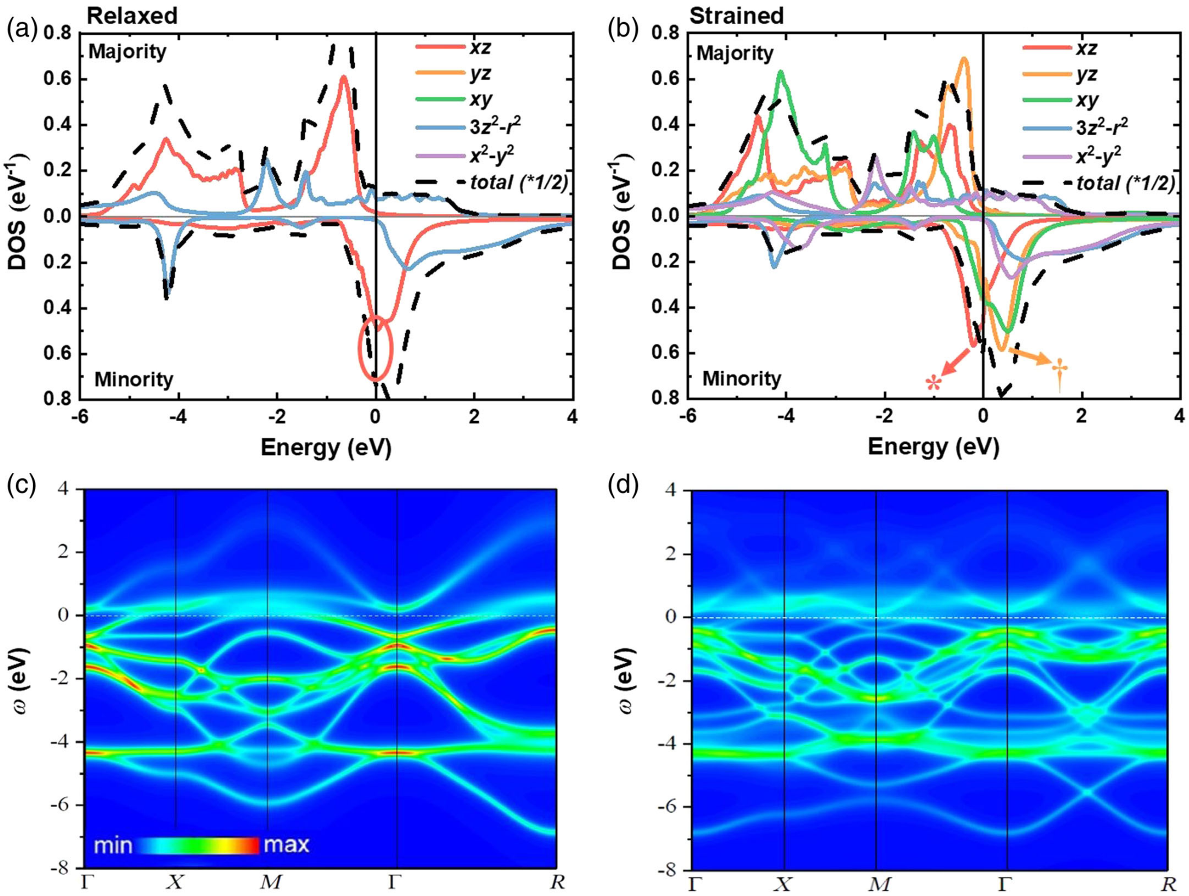

FIG. 4. Evolution of the electronic band structures for strained $SrCoO_3$ thin films with DFT + DMFT. Spin-resolved projected density of states (DOS) spectra for (a) the relaxed $SrCoO_3$ and (b) the strained $SrCoO_3$ (4% with xz/yz alternating splitting $\Delta\varepsilon = 0.1$ eV). The arrows highlight a clear splitting inside minority bands (* for minority xz band and † for minority yz band) at the Fermi level for the strained $SrCoO_3$ as compared with nonsplitting in relaxed $SrCoO_3$ marked by a red circle. The suppression of the spectral weight at the Fermi level is more clearly seen by comparing the electronic band dispersion for (c) the relaxed and (d) the strained $SrCoO_3$.

calculations. As shown in Fig. 4(a), our spin-resolved density of states (DOS) for relaxed $SrCoO_3$ is quantitatively consistent with the previous calculated result [13]. In contrast to the nearly fully occupied majority spin states, minority spin states are partially occupied and make a primary contribution to the electric conductance, in which the Fermi level crosses mainly at the Co t_{2g} states for relaxed $SrCoO_3$. The orbital occupancy of the fully relaxed sample obtained with our DFT + DMFT is indeed qualitatively in agreement with our DFT results [see Supplemental Material Figs. S7(a) and S7(b) [22]]. On the other hand, in tensile strained samples, the orbital degeneracy in t_{2g} states (xz, yz, vs xy) and in e_g states (x^2-y^2 vs $3z^2-r^2$) is expected to be lifted. Indeed, both DFT and DFT + DMFT results show such degeneracy lifting (see Supplemental Material Figs. S7(a) and S7(b) [22]), while the total Co3d occupation and the ordered Co moments are only weakly dependent on the strain (see Supplemental Material Figs. S7(c) and S7(d) [22]). The degeneracy lifting is much larger in the DFT + DMFT calculation, giving a stronger strain-dependent orbital polarization. Under 4% tensile strain, the orbital splitting is so strong in the minority spin states that the Fermi level crosses primarily at xz and yz bands in DFT + DMFT data, while in DFT data the Fermi level crosses at xz, yz, and xy bands nearly equally [see Supplemental Material Figs. S8(a)–S8(d) for comparison [22]], i.e., orbital polarization is amplified by correlation effects [30–32]. This would result in one electron occupation in the twofold degenerate minority spin xz and yz orbitals, and potentially lead to the cooperative Jahn-Teller effect accompanied by alternating spatial arrangement of xz and yz orbitals. To simulate this situation, we introduce a tiny potential splitting between the xz and yz orbitals, $\Delta\varepsilon = 0.1$ eV, and carry out a DFT + DMFT calculation. As shown in Fig. 4(b), the tiny splitting is enough to separate the xz and yz bands at the Fermi level as marked by arrows. The difference in the transport property could be explained more clearly in momentum-resolved spectral functions as shown in Figs. 4(c) and 4(d). The spectral intensity at the

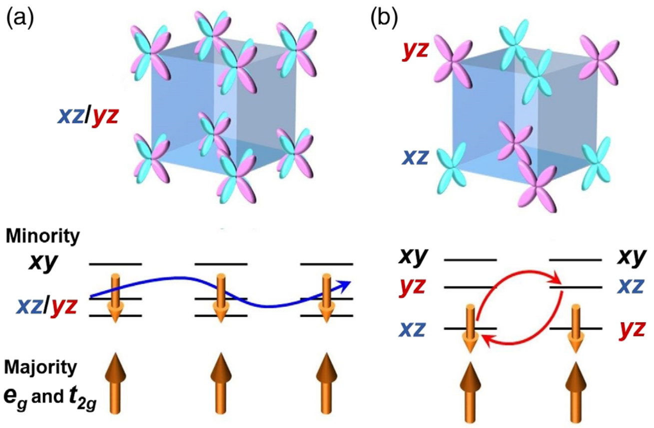

FIG. 5. Schematics of orbital structure and its correlation with ferromagnetic ground state. (a) Unstrained (or low strained) $SrCoO_3$ with twofold degenerate xz and yz bands, and (b) highly strained $SrCoO_3$ with alternating xz/yz orbital ordering. In (a), mobile minority electrons in the xz/yz band mediate double-exchange FM interaction. In (b), on the other hand, the virtual excitation of minority electrons from occupied xz (yz) orbital to neighboring unoccupied xz (yz) orbital induces Kugel-Khomskii-type FM superexchange interaction.

Fermi level is suppressed in the strained sample with such a small perturbation (0.1 eV), which could be regarded as a precursor of the electron localization. However, even with such a splitting inside minority bands, the FM ordering remains stable, and the ordered moment is barely changed.

Here, in contrast to the metallic state at unstrained or low-strained $SrCoO_3$ with the xz/yz degeneracy, where the FM interaction is mediated by the double-exchange interaction due to mobile minority electrons [Fig. 5(a)], the superexchange interaction with the alternating xz/yz ordering is responsible for the FM coupling due to the Kugel-Khomskii mechanism [33], as schematically shown in Fig. 5(b). We note that a similar FM interaction is realized in lightly doped CMR manganite [34]. This picture strongly contrasts with the previously predicted AFM ground state by first-principles calculations [15]. Indeed, using DFT, we confirm that AFM ordering is also more stable than FM ordering for the 4% strained sample by 0.36 eV per formula unit, which is accompanied by the change of the electron occupation N and the spin moment M on Co3d states from $N \approx 6.8$ and $M \approx 2.9\ \mu_B$ at FM to $N \approx 6.7$ and $M \approx 3.1\ \mu_B$ at AFM in DFT (both are close to the IS state at $d^{6.5\sim7}$). These differences become even larger in our DFT + DMFT calculations; $N \approx 6.4$ and $M \approx 2.7\ \mu_B$ at FM (IS state at $d^{6.5}$) and $N \approx 6$ and $M \approx 3.7\ \mu_B$ at AFM (HS state at d^6). This drastic change of N and M comes from the fact that intermediate-spin states, in which both t_{2g} and e_g orbitals are partially filled, are unstable compared with low-spin and high-spin states in the atomic limit [35]. This energetics might be overlooked in the DFT calculations, and the comparison of the total energy between different spin states as well as the examination of the xz/yz orbital ordering within the DFT + DMFT framework are desirable but left for future studies.

III. SUMMARY

To summarize, this work demonstrates a robust FM state in $SrCoO_3$ thin films under tensile strain beyond the critical strain value above which a transition from FM to AFM was predicted. We found the coexistence of the ferromagnetism and insulating transport behavior in highly strained samples, indicating a different mechanism being responsible for the FM ordering in the strained thin films rather than the Zener's double-exchange mechanism. Based on the DFT + DMFT calculations indicating strong orbital polarization under strain, we propose orbital ordering to induce the FM superexchange interaction with the splitting inside minority bands, which might finally cause a full gap. Furthermore, these results clearly highlight the importance of excellent oxygen stoichiometry for the studies of strained engineered complex oxides.

IV. METHODS

A. Synthesis of high-quality $SrCoO_3$ thin films

Brownmillerite $SrCoO_{2.5}$ thin films are grown by a customized reflection high-energy electron diffraction (RHEED) assisted pulsed laser deposition system, at a growth temperature of 750 °C and oxygen pressure of 0.125 mbar. The laser energy (KrF, $\lambda = 248$ nm) is fixed at 1.1 J/cm^2 with the repetition rate of 2 Hz. After the growth, the samples are cooled down to room temperature at a cooling rate of 10 °C/ min with 0.125-mbar oxygen to achieve high-quality epitaxial $SrCoO_{2.5}$ thin films with the thickness of ~30 nm. The sample thickness is confirmed with the x-ray reflectometry measurements, and the crystalline structures of thin films are characterized by a high-resolution four-circle x-ray diffractometer (Smartlab, Rigaku). The films are then postannealed in a chamber filled with 1 bar mixed ozone (5 g/m^3) and oxygen with the flow rate of 0.5 L/ min at 300 °C for 40 min, which nicely triggers the phase transformation from brownmillerite $SrCoO_{2.5}$ into perovskite $SrCoO_3$.

B. High-resolution scanning transmission electron microscopy characterization

The atomic-scale crystalline structures of the highly strained $SrCoO_3$ thin films are characterized with a high-resolution scanning transmission electron microscope (STEM, ARM-200CF, JEOL) operated at 200 keV and equipped with double spherical aberration (Cs) correctors.

C. Electrical transport and magnetic property measurements

A physical property measurement system (PPMS, Quantum Design) with lock-in amplifiers (Model SR830 DSP, Stanford research systems) is employed to measure the temperature-dependent resistivity, in which the four-probe method is employed to eliminate the contact resistance. Temperature-dependent magnetization is measured using a magnetic property measurement system (MPMS 3, Quantum Design) with the temperature ramping up from 4 to 300 K after a 2 T field cooling. In order to avoid the influence of the strong paramagnetic signal from the $DyScO_3$ substrate, we measure the remnant magnetization with zero field, while for other measurements, the magnetic field of 2 T is applied during the measurements.

D. Optical conductivity measurement

The reflectivity spectra are measured at room temperature with a spectrometer (Bruker IFS66v, Jasco MSV370), which covers the visible and infrared range with the energy from 0.3 to 3 eV. For this measurement, thin films are prepared on double-side polished substrates. To obtain enough optical intensity, we use slightly thicker samples with the thickness of ~50 nm as compared with other measurements. The optical conductivity spectra are derived by Kramers-Kronig analysis on the basis of the two-layer model.

E. X-ray absorption measurements

Soft x-ray absorption spectra (XAS) at Co L edges and O K edge are carried out at beam lines 4.0.2 and 6.3.1 of the Advanced Light Source with both total electron yield (TEY) mode and luminescence yield (LY) mode and then confirmed at beam line I06 of Diamond Light source with TEY and fluorescence yield (FY) modes and at BL25SU of SPring-8 with only TEY mode. The XAS spectra are normalized to the photon flux measured with the photocurrent from a clean gold mesh. For the x-ray magnetic circular dichroism (XMCD) measurements, the incident angle is fixed at 60°, the magnetic field (2 T) is applied along the beam incident direction, and a circularly polarized x ray is employed. The XAS spectra presented in this work are taken at 300 K, while the XMCD spectra are taken from 3 to 300 K, and then normalized by the polarization of the used circularly polarized x-ray. For the TEY mode, the signal is obtained by collecting the total electron yield current from the sample, which is therefore a surface-sensitive technique. While for the FY (LY) mode, the signal is a collection of the fluorescence (luminescence) intensity from the whole sample, and therefore is bulk sensitive. It is worth noting that due to the self-absorption effect of FY, we observe clearly different L_2/L_3 peak ratios between FY and TEY modes.

F. Electronic structure calculations

We carry out density functional theory (DFT) calculations using the Vienna *ab initio* simulation package (VASP) [36] with the projector augmented-wave method [37] and the Perdew-Burke-Ernzerhof (PBE) exchange-correlation functional [38]. We use for Co and O, standard potentials (Co and O in the VASP distribution) and for Sr a potential in which s states are treated as a valence states (Sr_{sv}). Structural optimization is performed using the Dudarev-type [39] on-site effective Coulomb interaction on Co d states with $U_{\mathrm{eff}} = U - J = 1.5$ eV ($U = 2.5$ eV and $J = 1.0$ eV) [16] with the FM spin polarization. A kinetic energy cutoff of 600 eV and a Monkhorst-Pack k mesh of $12 \times 12 \times 12$ are used for the plane-wave expansion of wave functions and k-space integration, respectively. The calculated equilibrium lattice constants are 3.834 Å, which is very close to the experimental value of 3.829 Å [7]. For strain-free cubic perovskite $SrCoO_3$, all the lattice parameters (a, b, c) are optimized, and for strained $SrCoO_3$ the c-axis lattice constant is optimized under ab-plane biaxial tensile strain of 1% to 4%.

In order to extract the parameters to describe the hopping between Co d and/or O p orbitals, maximally localized Wannier functions are further constructed with the WANNIER90 code [40] using non-spin-polarized PBE-only wave functions calculated on the above-optimized structures. Fourteen Wannier functions are thus obtained corresponding to the five d orbitals on one Co cation and the nine p orbitals on three equivalent O anions. The spreads of the Wannier functions are all smaller than 1 Å^2.

For comparison with DFT + DMFT results, additional DFT calculations are carried out using the optimized structure as mentioned above. An on-site effective Coulomb interaction on Co d states is taken as $U_{\mathrm{eff}} = 5.4$ eV [41], which gives the better agreement with the experiment and DFT + DMFT results in terms of ordered Co moments. Orbital-resolved Co d charge density and magnetization are computed from the local density of states projected onto Co d shells within the Wigner-Seitz radius of 1.302 Å.

DMFT calculations are performed using an effective model expressed as $H = H_{\mathrm{band}} + \sum_{i \in \mathrm{Co}\, d} H_{\mathrm{int},i}$. The band part H_{band} is given by

$$H_{\mathrm{band}} = \sum_{\mathbf{k}\sigma} \left[\hat{d}^{\dagger}_{\mathbf{k}\sigma}, \hat{p}^{\dagger}_{\mathbf{k}\sigma}\right] \begin{bmatrix} \hat{\varepsilon}^{dd}_{\mathbf{k}} - \varepsilon_{DC}\hat{1} & \hat{\varepsilon}^{dp}_{\mathbf{k}} \\ \hat{\varepsilon}^{pd}_{\mathbf{k}} & \hat{\varepsilon}^{pp}_{\mathbf{k}} \end{bmatrix} \begin{bmatrix} \hat{d}_{\mathbf{k}\sigma} \\ \hat{p}_{\mathbf{k}\sigma} \end{bmatrix}.$$

Here, $\hat{d}_{\mathbf{k}\sigma}(p_{\mathbf{k}\sigma})$ is a vector consisting of annihilation operators of Co d (O p) electrons with spin σ and momentum $\mathbf{k}$. Matrices $\hat{\varepsilon}^{\alpha\beta}_{\mathbf{k}}$ are the momentum-dependent hybridization functions in the Wannier basis obtained in the DFT calculations. α and β run through Co d and O p states. ε_{DC} is so-called double-counting correction, which subtracts Hartree-type Coulomb repulsion effects already included within DFT calculations. The interaction part $H_{\mathrm{int},i}$ is formally expressed as $H_{\mathrm{int},i} = \sum_{\alpha,\beta,\gamma,\delta} U_{\alpha\beta\gamma\delta} d^{\dagger}_{i\alpha} d^{\dagger}_{i\beta} d_{i\delta} d_{i\gamma}$ with $\alpha, \beta, \gamma, \delta$ indexing both spin and orbital on the Co d shell. Coulomb interaction $U_{\alpha\beta\gamma\delta}$ is expressed in terms of Slater integrals $F^{0,2,4}$. Taking the screened Coulomb interaction $U(= F^0) = 10$ eV and exchange interaction $J = 1$ eV [42] with $F^4/F^2 = 5/8$ [43], we determine $F^2 = 8.615$ eV and $F^4 = 5.385$ eV. The DMFT procedure maps this interacting lattice model into an interacting impurity model consisting of interacting Co d states and the effective hybridization that will be solved self-consistently [44]. To solve the impurity model, we use the hybridization-expansion version of the continuous-time quantum Monte-Carlo method [45] at $T = 0.02$ eV $= 232$ K. We keep only density-density components of $U_{\alpha\beta\gamma\delta}$ so that the efficient segment algorithm is utilized [46].

For the double-counting correction ε_{DC}, we use the procedure proposed in Ref. [47]:

$$\varepsilon_{DC} = \frac{1}{N_d} Re \sum_{\alpha} \Sigma_{\alpha}(i\omega_n \to i\infty).$$

Here, N_d is the number of Co d orbital times 2 (spin), i.e., 10. $\Sigma_{\alpha}(i\omega_n)$ is the Co d electron self-energy as a function of fermionic Matsubara frequency $\omega_n = (2n+1)\pi T$. Using this formula, ε_{DC} is updated at each DMFT iteration. This method has been successfully applied to describe metallic systems [47]. The electron spectral functions are computed using the self-energy that is analytically continued to the real frequency axis by the maximum entropy method [48].

ACKNOWLEDGMENTS

This study was financially supported by the Basic Science Center Project of National Natural Science Foundation of China (NFSC) under Grant No. 51788104; the National Natural Science Foundation of China (Grant No. 51872155); the National Basic Research Program of China Grant No. 2016YFA0301004; the Beijing Advanced Innovation Center for Future Chip (ICFC); and Engineering and Physical Sciences Research Council with grant reference EP/N016718/1. This research used resources of the Advanced Light Source, which is a DOE Office of Science User Facility under Contract No. DE-AC02-05CH11231. The research at O. R. N. L. was supported by U.S. DOE, Office of Science, Basic Energy Sciences, Materials Sciences and Engineering Division. N. P. L. acknowledges support from the National Natural Science Foundation of China (Grant No. 11974401), the Hundred Talents Program of the Chinese Academy of Science of China, and the Strategic Priority Research Program of the Chinese Academy of Sciences of China (No. XDB300000000).

[1] K. J. Choi, M. Biegalski, Y. L. Li, A. Sharan, J. Schubert, R. Uecker, P. Reiche, Y. B. Chen, X. Q. Pan, V. Gopalan, L.-Q. Chen, D. G. Schlom, and C. B. Eom, *Enhancement of Ferroelectricity in Strained* $BaTiO_3$ *Thin Films*, Science **306**, 1005 (2004).

[2] A. Sadoc, B. Mercey, C. Simon, D. Grebille, W. Prellier, and M.-B. Lepetit, *Large Increase of the Curie Temperature by Orbital Ordering Control*, Phys. Rev. Lett. **104**, 046804 (2010).

[3] J.-P. Locquet, J. Perret, J. Fompeyrine, E. Machler, J. W. Seo, and G. Van *Tendeloo, Doubling the Critical Temperature of* $La_{1.9}Sr_{0.1}CuO_4$ *Using Epitaxial Strain*, Nature (London) **394**, 453 (1998).

[4] J. H. Lee *et al.*, *A Strong Ferroelectric Ferromagnet Created by Means of Spinlattice Coupling*, Nature (London) **466**, 954 (2010).

[5] J. H. Haeni, P. Irvin, W. Chang, R. Uecker, P. Reiche, Y. L. Li, S. Choudhury, W. Tian, M. E. Hawley, B. Craigo, A. K. Tagantsev, X. Q. Pan, S. K. Streiffer, L. Q. Chen, S. W. Kirchoefer, J. Levy, and D. G. Schlom, *Room-Temperature Ferroelectricity in Strained* $SrTiO_3$, Nature (London) **430**, 758 (2004).

[6] R. J. Zeches *et al.*, *A Strain-Driven Morphotropic Phase Boundary in* $BiFeO_3$, Science **326**, 977 (2009).

[7] Y. W. Long, Y. Kaneko, S. Ishiwata, Y. Taguchi, and Y. Tokura, *Synthesis of Cubic* $SrCoO_3$ *Single Crystal and Its Anisotropic Magnetic and Transport Properties*, J. Phys. Condens. Matter **23**, 245601 (2011).

[8] M. Hoffmann, V. S. Borisov, S. Ostanin, I. Mertig, W. Hergert, and A. Ernst, *Magnetic Properties of Defect-Free and Oxygen-Deficient Cubic* $SrCoO_{3-\delta}$, Phys. Rev. B **92**, 094427 (2015).

[9] C. Zener, *Interaction between the d-Shells in the Transition Metals. II. Ferromagnetic Compounds of Manganese with Perovskite Structure*, Phys. Rev. **82**, 403 (1951).

[10] R. H. Potze, G. A. Sawatzky, and M. Abbate, *Possibility for an Intermediate-Spin Ground State in the Charge-Transfer Material* $SrCoO_3$, Phys. Rev. B **51**, 11501 (1995).

[11] M. Zhuang, W. Y. Zhang, A. Hu, and N. B. Ming, *Possible Magnetic Ground State in the Perovskite* $SrCoO_3$, Phys. Rev. B **57**, 13655 (1998).

[12] G. Kotliar, S. Y. Savrasov, K. Haule, V. S. Oudovenko, O. Parcollet, and C. A. Marianetti, *Electronic Structure Calculations with Dynamical Mean-Field Theory*, Rev. Mod. Phys. **78**, 865 (2006).

[13] J. Kunes, V. Krapek, N. Parragh, G. Sangiovanni, A. Toschi, and A. V. Kozhevnikov, *Spin State of Negative Charge-Transfer Material* $SrCoO_3$, Phys. Rev. Lett. **109**, 117206 (2012).

[14] J. H. Lee and K. M. Rabe, *Epitaxial-Strain-Induced Multiferroicity in* $SrMnO_3$ *from First Principles*, Phys. Rev. Lett. **104**, 207204 (2010).

[15] J. H. Lee and K. M. Rabe, *Coupled Magnetic-Ferroelectric Metal-Insulator Transition in Epitaxially Strained* $SrCoO_3$ *from First Principles*, Phys. Rev. Lett. **107**, 067602 (2011).

[16] J. H. Lee and K. M. Rabe, *Large Spin-Phonon Coupling and Magnetically Induced Phonon Anisotropy in* $SrMO_3$ *Perovskites* ($M = V$*, Cr, Mn, Fe, Co)*, Phys. Rev. B **84**, 104440 (2011).

[17] S. J. Callori, S. Hu, J. Bertinshaw, Z. J. Yue, S. Danilkin, X. L. Wang, V. Nagarajan, F. Klose, J. Seidel, and C. Ulrich,

Strain-Induced Magnetic Phase Transition in $\mathrm{SrCoO}_{3-\delta}$ *Thin Films*, Phys. Rev. B **91**, 140405(R) (2015).

[18] J. R. Petrie, C. Mitra, H. Jeen, W. S. Choi, T. L. Meyer, F. A. Reboredo, J. W. Freeland, G. Eres, and H. N. Lee, *Strain Control of Oxygen Vacancies in Epitaxial Strontium Cobaltite Films*, Adv. Funct. Mater. **26**, 1564 (2016).

[19] S. B. Hu, Y. Wang, C. Cazorla, and J. Seidel, *Strain-Enhanced Oxygen Dynamics and Redox Reversibility in Topotactic* $\mathrm{SrCoO}_{3-\delta}$ *(*$0 < \delta \leq 0.5$*)*, Chem. Mater. **29**, 708 (2017).

[20] Y. D. Gu, C. Song, H. R. Zhang, Z. C. Wang, B. Cui, F. Li, J. J. Peng, M. S. Saleem, G. Y. Wang, X. Y. Zhong, F. Wang, S. Ma, J. R. Sun, W. Liu, F. Pan, and Z. D. Zhang, *Controllable Oxygen Vacancies, Orbital Occupancy, and Magnetic Ordering in* $\mathrm{SrCoO}_{3-\delta}$ *Films*, J. Magn. Magn. Mater. **454**, 228 (2018).

[21] J. W. Guo, P. S. Wang, Y. Yuan, Q. He, J. L. Lu, T. Z. Chen, S. Z. Yang, Y. J. Wang, R. Erni, M. D. Rossell, V. Gopalan, H. J. Xiang, Y. Tokura, and P. Yu, *Strain-Induced Ferroelectricity and Spin-Lattice Coupling in* SrMnO_3 *Thin Films*, Phys. Rev. B **97**, 235135 (2018).

[22] See Supplemental Material at http://link.aps.org/supplemental/10.1103/PhysRevX.10.021030 for more details about structural characterization, XAS-based measurements and calculation.

[23] N. P. Lu *et al.*, *Electric-Field Control of Tri-State Phase Transformation with a Selective Dual-Ion Switch*, Nature (London) **546**, 124 (2017).

[24] H. Jeen, W. S. Choi, M. D. Biegalski, C. M. Folkman, I.-C. Tung, D. D. Fong, J. W. Freeland, D. Shin, H. Ohta, M. F. Chisholm, and H. N. Lee, *Reversible Redox Reactions in an Epitaxially Stabilized* SrCoO_x *Oxygen Sponge*, Nat. Mater. **12**, 1057 (2013).

[25] C. T. Chen, Y. U. Idzerda, H.-J. Lin, N. V. Smith, G. Meigs, E. Chaban, G. H. Ho, E. Pellegrin, and F. Sette, *Experimental Confirmation of the X-Ray Magnetic Circular Dichroism Sum Rules for Iron and Cobalt*, Phys. Rev. Lett. **75**, 152 (1995).

[26] D. Zhang, H. Ishizuka, N. P. Lu, Y. J. Wang, N. Nagaosa, P. Yu, and Q.-K. Xue, *Anomalous Hall Effect and Spin Fluctuations in Ionic Liquid Gated* SrCoO_3 *Thin Films*, Phys. Rev. B **97**, 184433 (2018).

[27] N. F. Mott, *Conduction in Glasses Containing Transition Metal Ions*, J. Non-Cryst. Solids **1**, 1 (1968).

[28] B. I. Shklovskii, *Variable-Range Hopping Conduction*, in *Electronic Properties of Doped Semiconductors*, Springer Series in Solid-State Sciences Vol 45 (Springer, Berlin, Heidelberg, 1984).

[29] M. Imada, A. Fujimori, and Y. Tokura, *Metal-Insulator Transitions*, Rev. Mod. Phys. **70**, 1039 (1998).

[30] E. Pavarini, S. Biermann, A. Poteryaev, A. I. Lichtenstein, A. Georges, and O. K. Andersen, *Mott Transition and Suppression of Orbital Fluctuations in Orthorhombic* $3d^1$ *Perovskites*, Phys. Rev. Lett. **92**, 176403 (2004).

[31] P. Werner and A. J. Millis, *High-Spin to Low-Spin and Orbital Polarization Transitions in Multiorbital Mott Systems*, Phys. Rev. Lett. **99**, 126405 (2007).

[32] H. Ishida and A. Liebsch, *Origin of Metallicity of* $\mathrm{LaTiO}_3/\mathrm{SrTiO}_3$ *Hetero-Structures*, Phys. Rev. B **77**, 115350 (2008).

[33] K. I. Kugel and D. I. Khomskil, *The Jahn-Teller Effect and Magnetism: Transition Metal Compounds*, Sov. Phys. Usp. **25**, 231 (1982).

[34] Y. Endoh, K. Hirota, S. Ishihara, S. Okamoto, Y. Murakami, A. Nishizawa, T. Fukuda, H. Kimura, H. Nojiri, K. Kaneko, and S. Maekawa, *Transition between Two Ferromagnetic States Driven by Orbital Ordering in* $\mathrm{La}_{0.88}\mathrm{Sr}_{0.12}\mathrm{MnO}_3$, Phys. Rev. Lett. **82**, 4328 (1999).

[35] Y. Tanabe and S. Sugano, *On the Absorption Spectra of Complex Ions II*, J. Phys. Soc. Jpn. **9**, 766 (1954).

[36] G. Kresse and J. Furthmuller, *Efficient Iterative Schemes for Ab InitioTotal-Energy Calculations Using a Plane-Wave Basis Set*, Phys. Rev. B **54**, 11169 (1996).

[37] G. Kresse and D. Joubert, *From Ultrasoft Pseudopotentials to the Projector Augmented-Wave Method*, Phys. Rev. B **59**, 1758 (1999).

[38] J. P. Perdew, K. Burke, and M. Ernzerhof, *Generalized Gradient Approximation Made Simple*, Phys. Rev. Lett. **77**, 3865 (1996).

[39] S. L. Dudarev, G. A. Botton, S. Y. Savrasov, C. J. Humphreys, and A. P. Sutton, *Electron-Energy-Loss Spectra and the Structural Stability of Nickel Oxide: An* LSDA + *U Study*, Phys. Rev. B **57**, 1505 (1998).

[40] A. A. Mostofi, J. R. Yates, G. Pizzi, Y.–S. Lee, I. Souza, D. Vanderbilt, and N. Marzari, *An Updated Version of* *WANNIER90: A Tool for Obtaining Maximally-Localised Wannier Functions*, Comput. Phys. Commun. **185**, 2309 (2014).

[41] H. Hsu and S.-C. Huang, *Simultaneous Metal-Half-Metal and Spin Transition in* SrCoO_3 *under Compression*, Phys. Rev. Mater. **2**, 111401(R) (2018).

[42] K. Haule, *Exact Double Counting in Combining the Dynamical Mean Field Theory and the Density Functional Theory*, Phys. Rev. Lett. **115**, 196403 (2015).

[43] F. M. F. de Groot, J. C. Fuggle, B. T. Thole, and G. A. Sawatzky, *2p X-Ray Absorption of* 3d *Transition-Metal Compounds: An Atomic Multiplet Description Including the Crystal Field*, Phys. Rev. B **42**, 5459 (1990).

[44] A. Georges, G. Kotliar, W. Krauth, and M. J. Rozenberg, *Dynamical Mean-Field Theory of Strongly Correlated Fermion Systems and the Limit of Infinite Dimensions*, Rev. Mod. Phys. **68**, 13 (1996).

[45] E. Gull, A. J. Millis, A. I. Lichtenstein, A. N. Rubtsov, M. Troyer, and P. Werner, *Continuous-Time Monte Carlo Methods for Quantum Impurity Models*, Rev. Mod. Phys. **83**, 349 (2011).

[46] P. Werner, A. Comanac, L. de' Medici, M. Troyer, and A. J. Millis, *Continuous-Time Solver for Quantum Impurity Models*, Phys. Rev. Lett. **97**, 076405 (2006).

[47] J. Braun, J. Minár, H. Ebert, M. I. Katsnelson, and A. I. Lichtenstein, *Spectral Function of Ferromagnetic* 3d *Metals: A Self-Consistent* LSDA + DMFT *Approach Combined with the One-Step Model of Photoemission*, Phys. Rev. Lett. **97**, 227601 (2006).

[48] M. Jarrell and J. E. Gubernatis, *Bayesian Inference and the Analytic Continuation of Imaginary-Time Quantum Monte Carlo Data*, Phys. Rep. **269**, 133 (1996).